Radiation Physics and Chemistry 179 (2021) 109103

Contents lists available at ScienceDirect

Radiation Physics and Chemistry

journal homepage: www.elsevier.com/locate/radphyschem

A low-cost small-size commercial PIN photodiode: I. Electrical characterisation and low-energy photon spectrometry

A.A. Malafronte[a], A.R. Petri[a], J.A.C. Gonçalves[b], S.F. Barros[a,c], C.C. Bueno[b], N.L. Maidana[a], A. Mangiarotti[a,*], M.N. Martins[a], A.A. Quivy[a], V.R. Vanin[a]

[a] Instituto de Física da Universidade de São Paulo, Rua do Matão 1371, 05508-090, São Paulo, Brazil
[b] Instituto de Pesquisas Energéticas e Nucleares, Comissão Nacional de Energia Nuclear, São Paulo, Brazil
[c] Instituto Federal de São Paulo, Rua Primeiro de Maio 500, Bairro Estação, 08571-050, Itaquaquecetuba, SP, Brazil

ARTICLE INFO

Keywords:
Silicon detector
Low-cost PIN diode
BPX 65
γ- and x-ray spectrometry

ABSTRACT

Silicon PIN (p-type-intrinsic-n-type) photodiodes are well suited as particle detectors. Here the interest is on a low-cost solution by repurposing a commercial device meant to be used as a light sensor. The intended application is to measure the energy spectra of electrons scattered by thin metallic foils covering small angles close to the beam of the accelerator. The main requirements for a suitable device are: 1) a low-cost solution to allow frequent replacements; 2) a small size to avoid as much as possible an unused area that contributes with unnecessary capacitance; 3) a good energy resolution; and 4) an easy repurposing as a charged-particle detector. The photodiode type BPX 65 manufactured by Osram® fulfils well these requirements. Four samples of these commercial devices have been electrically characterised with respect to reverse current and depleted-region capacitance. At the selected working point of 18 V, comfortably below the maximum rating of 20 V recommended by the manufacturer for continuous operation, the total thickness of the depleted and intrinsic regions is estimated to be (60 ± 3) μm. For the four samples considered, the measured reverse currents for a reverse bias of 18 V are around 0.1 nA, well below the typical value specified by the manufacturer (1 nA). To evaluate the performance of the device as a detector, energy spectra have been acquired for γ-rays with energies from 10 to 140 keV using ^{241}Am, ^{133}Ba, and ^{57}Co radioactive sources. The resolution of the BPX 65 encountered with the γ-rays emitted by ^{241}Am at 59.5-keV is ≈ 2.5 keV (FWHM - Full Width at Half Maximum), which is close to the value obtained with a pulser, showing that its main limitation is the electronic chain employed in the setup. The response function to monoenergetic electrons in the same energy range is studied in the companion paper.

1. Introduction

Solid-state semiconductor detectors are widely used for spectral measurement of both photons and charged particles (e.g. Si(Li) detectors, high purity germanium (HPGe) detectors, surface barrier detectors, passivated implanted planar silicon (PIPS) detectors, and silicon drift detectors (SDD), among others) as well as for tracking (e.g. charge coupled devices (CCD), silicon microstrip detectors, and silicon pixel detectors, among others) due to their ruggedness, ease of deployment, compactness, good resolution, and insensitivity to magnetic fields. Moreover, the great advance of microelectronic technologies allows for an almost endless range of designs and customizations. Three main approaches are possible in the search for a detector suited to a particular experimental setup: *i*) design of an application-specific sensor; *ii*) adoption of a commercial detector; and *iii*) repurposing of a device designed for a completely different application. For reasons of availability of the necessary knowledge, manpower, and costs, the first choice is mostly restricted to large collaborations. Smaller groups are therefore forced, in most cases, to select between the second and third options. The economical aspect can then become a decisive factor, in particular if many similar channels are needed. Even when few channels are necessary, eventually one, the aspect of cost can still be of paramount importance if frequent replacements are anticipated due to radiation damage. This last condition is particularly relevant when measurements have to be conducted on direct beams from particle accelerators or very intense radioactive sources. Thus, repurposing a device developed for a different use, like a diode or a photodiode, can become very competitive, if a suitable low-cost one can be found. This

* Corresponding author.
E-mail address: alessio@if.usp.br (A. Mangiarotti).

https://doi.org/10.1016/j.radphyschem.2020.109103
Received 11 March 2020; Received in revised form 5 July 2020; Accepted 9 July 2020
Available online 19 August 2020
0969-806X/

is precisely the condition we are concerned within the present work.

Among all diodes, the ones manufactured with a PIN (p-type-intrinsic-n-type) structure are very attractive because, especially those designed to be used as photodiodes, have a planar geometry with a large central area where the electric field is uniform and a good charge collection can be anticipated. Moreover, the presence of an intrinsic layer results in a large depleted region, which is the one mostly contributing to the generation of the signal, capable of containing the range of several primary or secondary charged particles with energies of interest for many applications in pure and applied physics. Such an approach has been pioneered over the years by few groups, see the publications by Kollewe (1987), Gooda and Gilboy (1987), Markevich et al. (1988), Yamamoto et al. (1988), Weinheimer et al. (1992), and Bueno et al. (1996), and has now turned quite common, see the works by Bueno et al. (2004), Zhao et al. (2016, 2018), and others cited therein. Tests of devices manufactured with semiconductors different from silicon, which is still the most common case, have also been reported by Zhao et al. (2016, 2018) (see the other publications cited therein as well). Custom-made detectors have been employed by Ahmad et al. (1990), Lee et al. (2016), and Wall et al. (2014): the last example, from the large collaboration KATRIN (KArlsruhe TRItium Neutrino), adopts a complex design with segmented pixels. Here the focus is on very common silicon photodiodes repurposed as particle detectors, because they are easily available in large quantities and at low prices from retailers of electronic components.

In general, such devices perform well for the measurement of energy spectra. For instance, a resolution (FWHM) of 1.8 keV for γ-rays of 59.5 keV from ^{241}Am was obtained by Bueno et al. (2004) with a Hamamatsu photodiode (S2506-04) at room temperature. By cooling at − 97 °C both the photodiode and the first stage of a special well-matched preamplifier, Weinheimer et al. (1992) could reach a record resolution of 1.1 keV at the same energy. PIN photodiodes have also been used in current mode for dose quantification by several groups for photons (Romei et al., 2015; Oliveira et al., 2016; Gonçalves et al., 2020) and electrons (Khoury et al., 1999, 2007) thanks to their good radiation tolerance and low cost. An interesting case is that of a beam profile monitoring system built stacking several two dimensional arrays of seven by seven photodiodes to cover a large area (Palni et al., 2014). However, the present work deals with measurements in pulse mode for energy determination.

Despite the several publications mentioned above, covering both low-cost PIN photodiodes and spectrometry, we could not find one suited to our particular setup where we need to measure the spectra of electrons with energies up to 100 keV, over a small solid angle, and very close to the accelerator beam. Therefore, we started a search among possible available options and found the BPX 65. The particular requirements and why they are satisfied by this choice are discussed in the next section. So far, the BPX 65 was applied previously only to studies on radiation damage induced by ions (Jakšić et al., 2005) and γ-rays (Jafari et al., 2018). Therefore, a full characterisation, both in electrical terms and as a detector, has been undertaken and is reported in the present paper (paper I) and in the companion one (paper II (Mangiarotti et al., 2020)). The former covers the electrical measurements and the tests with photons of energies up to 140 keV. In the latter, a direct monoenergetic beam from an accelerator has been employed to investigate the response function to electrons.

The present paper is organised as follows. Section 2 motivates the choice of the BPX 65 and describes the setups used for its electrical characterisation and for its testing with photons. The results obtained are presented in Section 3, including the spectra collected employing radioactive sources emitting photons with energies from 14 to 140 keV and the analysis of the resolution. The overall performance of the BPX 65 is discussed critically in Section 4. Finally, the conclusion is drawn in Section 5.

2. Materials and methods

2.1. Choice of a device

The application of concern here is the measurement of the angular distributions resulting from the multiple scattering of electrons with energies between 10 and 100 keV from thin metallic foils, whose requirements are the following.

1. It must be placed as close as possible to the accelerator beam to scan the largest possible part of the angular distribution reaching down to very forward angles. This demands a low-cost solution to allow frequent replacements because high-radiation doses can be anticipated during normal use or in case of accidental mispositioning of the diode in the beam.
2. The detector is employed with a collimator to define very well the solid angle of the impinging electrons. Considering the practical limitation on the distance from target of about 25 cm, a typical diameter of the hole in the collimator is below 0.5 mm. Therefore, a large active area is not desirable, since it increases the capacitance and, as a consequence, results in loss of resolution, without any contribution to the efficiency, because it remains shielded from the radiation. The collimator also helps to reduce the count rate at frontal angles. At backward angles, the count rates can be increased by using higher beam currents.
3. A good energy resolution is important to separate electrons that are deflected in the target from those that are the product of more complicated interaction histories and loose energy in other parts of the setup.
4. Finally, (although not strictly necessary) the device should be easy to repurpose for its final use. Because electrons have to be measured, the silicon chip of the photodiode has to be exposed to the vacuum of the chamber. Thus, in the case of plastic casings, they would have to be chemically removed and the PIN photodiode would have to be mounted on a new support.

All these requirements lead us to choose the BPX 65, a silicon photodiode with a square area of 1 mm^2 and a TO-18 metallic casing. The area of the chip is well matched to that of the anticipated collimator, avoiding the presence of a large unused part. Moreover, the manufacturer declares a low reverse current that contributes to the reduction of the electronic noise. The optical window can straightforwardly be removed by thinning the edges of the metallic casing. The retail cost of the BPX 65 is about one hundredth of that of a surface barrier or PIPS detector from commercial suppliers with few times the area and a slightly worse resolution (according to tests conducted by us in our setup).

However, two main aspects need to be considered and thoroughly tested when repurposing a PIN photodiode as a detector.

i. The chip has an optical coating, to avoid reflection of light, an ohmic contact, and an undepleted region that result in a dead and partially dead entrance layers. This is an important disadvantage when compared, for example, to PIPS detectors, manufactured with a special technology to have a very thin surface contact, which is of paramount importance for heavier charged particles and, in particular, for fission fragments. However, for electrons with energies between 10 and 100 keV, that are considerably scattered inside the detector and have a lower energy loss per unit of path length, the impact of these top layers is small. The thickness of the dead layer has been investigated in paper II and found to be equivalent to few hundred nm of silicon.
ii. Because the device is not meant to be used as a particle detector, the guard ring structure can be absent, resulting in a non uniform electric field (and hence charge collection) close to the border of the active area. As a matter of fact, early investigations by Gooda and

Gilboy (1987) on repurposing of commercial PIN photodiodes for α spectrometry found the presence of spurious secondary peaks, displaced at a lower channel number from the main one, due to particles impinging close to the borders and attributed these structures to non uniformities of the charge-collection efficiency or of the thickness of the optical coating. Moreover, the absence of the guard ring can result in increased reverse currents so that, again, in early investigations, Yamamoto et al. (1988), placed silicon grease around the chip to improve the insulation. By visual inspection, it seems that at least an incomplete guard ring is present on the BPX 65. Unfortunately, the datasheet by the manufacturer does not provide any information on the detailed structure of the device. All the tests described in the present paper I and in paper II have not shown any evidence of the mentioned problems at the selected working point.

From the previous comments, it is rather clear that the repurposing of a particular PIN photodiode demands a careful characterisation both in electrical terms and with radiation. It is to such a task that the present paper I and the companion paper II are devoted.

2.2. Electrical characterisation

The particular four samples of the BPX 65 PIN silicon photodiodes employed for the tests described in the present paper I and in the companion paper II have been manufactured by Osram®. There are other companies on the market, but they may possibly produce devices with slightly different parameters from those described here. The geometrical area of the chip is 1 mm^2, as previously mentioned. The reverse bias of a PIN diode operating as a radiation detector must be chosen considering the total width of its depleted and intrinsic regions (which is related to its capacitance) and its reverse current. Therefore, they have been studied using a Semiconductor Device Parameter Analyser (model B1500A by Agilent®).

The depleted-region capacitance (Millman and Halkias, 1972) C_T of the BPX 65 has been determined for a range of applied reverse biases from 0 to 25 V, at room temperature. The frequency used to measure the capacitance with the B1500A has been set to 1.0 MHz. The Semiconductor Device Parameter Analyser allows to remove, by proper calibration measurements, the parasitic capacitance of the cables. To confirm the protocol, it has been verified that, indeed, their value is constant, within the accuracy of the B1500A, as a function of the applied voltage. However, the parasitic capacitance C_{TO} of the TO-18 metallic casing is still included. Thus, one extra sample of the BPX 65 has been employed with the bond wire removed in order to obtain C_{TO}. Again, for consistency, it has been verified that, within the accuracy of the B1500A, C_{TO} does not depend on the bias voltage.

A PN step graded junction is a junction where the acceptor and donor number densities, N_A and , are constant on the p- and n-sides, respectively, and change abruptly at the interface (Millman and Halkias, 1972). The width of the depleted region, W, in a PN step graded junction is related to the capacitance C_T as (Millman and Halkias, 1972)

$$W = \frac{\varepsilon A}{C_T} , \tag{1}$$

where ε is the dielectric permittivity of silicon and A is the active area of the diode. Eq. (1) remains valid for a linearly graded PN junction (Millman and Halkias, 1972) or for a PIN step graded junction, where now W is the sum of the widths of the depleted regions on the p- and n-sides and of the width of the intrinsic region.

Within the model of a PIN step graded junction, the total widths of the depleted and intrinsic regions, W, can be shown to be

$$W = \sqrt{d^2 + \frac{2\,\varepsilon}{e}\,\frac{N_A + N_D}{N_A\,N_D}\,(V_0 - V_d)} , \tag{2}$$

where d is the width of the intrinsic region, V_0 is the contact potential of the PIN junction, V_d is the applied voltage (which is negative for a reverse bias), and e is the unit of elementary charge. Indicating the width of the depleted and intrinsic layers at 0 V as W_0, Eq. (2) can be rewritten as

$$W = W_0 \sqrt{1 - \frac{V_d}{V'}} , \tag{3}$$

where V' is a parameter related to the acceptor and donor densities and to the width of the intrinsic region.

2.3. Photon spectroscopy

To characterise the device as a radiation detector, a special setup has been developed and used with radioactive sources. Since the duration of the measurements is of few days, the issue of the stability in time is important. Each of these topics is discussed in separated items.

2.3.1. Setup and electronic chain

A BPX 65, with the entrance window of the TO-18 casing removed, is exposed without a collimator, representing the worst-case scenario for edge effects. The detector, held by an aluminium disc, is supported at a distance of approximately 20 mm from a radioactive source inside a stainless steel vacuum chamber. Even though the temperature is not controlled, fluctuations are limited to about 1 °C accompanying the environmental changes in our underground experimental room. The BPX 65 is AC coupled to an Amptek® A250 charge-sensitive preamplifier located very close inside the stainless steel chamber. The output of the A250 is then processed by an amplifier (model 572 by Ortec®) with a shaping time constant of 2 μs and a gain of approximately 800. Finally, the signal is acquired by a multi-channel analyser (model 927 Aspec by Ortec®).

2.3.2. Radioactive sources

To test the BPX 65 as a radiation detector, three radioactive sources have been employed: ^{241}Am, ^{133}Ba, and ^{57}Co.

The ^{241}Am source has been manufactured at IPEN/CNEN-SP (Instituto de Pesquisas Energéticas e Nucleares, Comissão Nacional de Energia Nuclear, São Paulo). A small quantity of a solution with an activity of about $2{\cdot}10^6$ Bq was deposited on a disk of polyethylene with a thickness of 0.5 mm and left exposed. The source is used with the radioactive material on the opposite side of the backing with respect to the BPX 65. Thus, the α particles from the decay of ^{241}Am can reach the detector only by crossing the polyethylene disk and are, therefore, stopped. Due to the employed geometry, the source can be considered as a pure γ- and x-ray emitter.

The ^{133}Ba and ^{57}Co sources have been manufactured and calibrated at LMN-IPEN/CNEN-SP (Laboratório de Metrologia Nuclear do Instituto de Pesquisas Energéticas e Nucleares, Comissão Nacional de Energia Nuclear, São Paulo). The deposited solutions are enclosed between one Kapton foil and a polyethylene support with thicknesses of 7.5 μm and 0.3 mm, respectively. These sources are used with the BPX 65 facing the Kapton foil, that allows electrons from internal conversion to escape. Their activities were $(5.60 \pm 0.17){\cdot}10^5$ Bq (^{133}Ba) and $(3.89 \pm 0.13){\cdot}10^5$ Bq (^{57}Co) at the time of the measurements.

2.3.3. Time stability

Collecting a good statistics requires between one and three days, since the typical count rate with the ^{241}Am, ^{133}Ba, and ^{57}Co sources just described is around 100 Hz. To monitor the time drift of the electronic chain, all the measurements presented here have been divided into runs of 2 h resulting in approximately 15–30 spectra. An Arbitrary Waveform Generator (model 33500 B by Agilent®), simulating a nuclear pulser, has been connected to the test input of the A250 and run at a rate of 40 Hz during the data taking. Then the pulser peak from each run has been fitted with a Gaussian to check for possible changes in the

position of the centroid and evaluate the contribution of noise to the resolution. In a few worst cases of all those considered for the present paper, a change of 0.1% (corresponding to ≈ 1 channel over the full range of 1024) has been observed, but the typical behaviour is better. Since even this 0.1% is much smaller than the resolution (see Section 3.5), it has been decided to avoid any correction. As a matter of fact, it is the main limitation in the accuracy of the calibration performed in the present work, see Section 3.4. A much better pulser capable of generating a sequence of different amplitudes would be needed to correct variations in both gain and offset.

2.3.4. Photon detection and peak shape model

The presence of an optical coating, an ohmic contact, and a possibly undepleted region at the top of the detector, as discussed in Section 2.1, do not affect significantly the response to photons. However, the limited total thickness of the depleted and intrinsic regions strongly influence its usability as a photon detector. For devices commercialised for such a purpose, typical values are of the order of several hundred μm. Moreover, as mentioned in Section 2.1, the possible absence of a well designed guard ring can result in a non uniform field at the borders of the device with the consequence of an incomplete charge collection and the appearance of spurious peaks (Gooda and Gilboy, 1987).

To assess the practical usability of the BPX 65, several spectra have been collected with the radioactive sources, either in vacuum or with the chamber filled with air. Absorbers made of Al with a thickness of 0.5 mm have been employed to stop the electrons and enhance the photon component of the spectra, when deemed necessary.

Different models for the observed x- and γ-rays peaks are adopted and their parameters fitted by a Least-Squares (LS) procedure. In the case of the emission at 59.5 keV from ^{241}Am (Bé et al., 2010), which is isolated from all others (see Fig. 7), a Gaussian is employed to model the peak

$$A_G \exp\left(-\frac{(x - x_G)^2}{2\,\sigma_G^2}\right), \tag{4}$$

where x is the channel of the spectrum, x_G the position of the peak, σ_G the standard deviation of the Gaussian, and A_G a normalisation constant. The continuum component below the peak is described by a second degree polynomial plus the convolution of a step with a Gaussian with the same standard deviation

$$A_S \operatorname{erfc}\left(\frac{x - x_G}{\sqrt{2}\,\sigma_G}\right) \tag{5}$$

where erfc is the complementary error function (Abramowitz and Stegun, 1972) and A_S another normalisation constant.

However, this is essentially the only simple case. In all others (i.e. 26.9 keV in ^{241}Am (Bé et al., 2010), 53.2 and 81.0 keV in ^{133}Ba (Bé et al., 2016) and 14.4, 122, and 136 keV in ^{57}Co (Bé et al., 2004)), since there are always not well separated closeby peaks, a simultaneous fit to all of them is performed to avoid a dependence of the results from the selected part of the spectrum. A term equal to Eq. (4) is added for each peak. Each Gaussian has, of course, a different position, $x_{G\,i}$, and a different width, $\sigma_{G\,i}$, allowing to extract the behaviour of the energy resolution. The continuum component below the multiple Gaussians is described by a second degree polynomial common to the whole spectrum plus a term like Eq. (5) added in correspondence of each peak. The fits have been performed with the C++ reimplementation of MINUIT (James and Roos, 1975) through the ROOT data analysis framework (Brun and Rademakers, 1997).

2.3.5. Energy calibration

The response of the detector as a function of photon energy E is evaluated using a linear relation

$$x = a + b\,E \tag{6}$$

with x the channel number. The parameters a and b are fitted to the peak positions of the γ-rays from the radioactive sources by a LS procedure. Photon energies are taken from the tabulations by Bé et al. (2010, 2016, 2004). The uncertainties on the energies of the selected lines E are much smaller than those on the peak positions obtained from the fit with the models described in Section 2.3.4 and can safely be neglected.

2.3.6. Energy resolution

As a matter of fact, the FWHM of the Gaussian introduced in Section 2.3.4, see Eq. (4), is universally employed to quote the resolution of an energy dispersive photon spectrometer. Three effects are known to contribute in semiconductor detectors (Knoll, 2010): noise from the electronic chain, fluctuations in the collection of the produced electron-hole pairs and fluctuations in their generation. This classical topic was investigated for Si(Li) and HPGe detectors by Hollstein (1970) and Owens (1985), respectively. The standard deviation of the Gaussian, σ_G, depends on the energy deposited in the depleted and intrinsic regions of the diode, E_{dep}, as (Hollstein, 1970; Owens, 1985; Scholze and Procop, 2001)

$$\sigma_G^2 = \sigma_{el}^2 + \sigma_{cc}^2 + w\,F\,E_{dep}\,, \tag{7}$$

where σ_{el} is the contribution from the electronic chain, σ_{cc} from charge collection, w the average energy spent to create an electron-hole pair, and F the Fano factor. Obviously, σ_{el} depends on the electronic chain employed but also on the capacitance and reverse current of the detector, while σ_{cc} is influenced by the electric field in the device and the locations where the electron-hole pairs are produced, which in turn are sensitive to the bias, the energy of the photons, and the geometry of the irradiation (Hollstein, 1970; Owens, 1985). With standard values of the parameters (w = 3.66 eV and F = 0.114 (Scholze and Procop, 2001) or w = 3.58 eV and F = 0.135 (Gao et al., 2007)), Eq. (7) predicts for the energy dependent part a value of 150–160 and 480–520 eV FWHM for E_{dep} = 10 and 100 keV, respectively.

2.3.7. Efficiency model

A simple estimate of the efficiency ε considering only the attenuation in the aluminium absorber (see section 2.3.4) and the photo-electric interactions in the active volume of the detector is given by

$$\varepsilon(E) = \Omega\, e^{-\mu_{Al}(E)\,t_{Al}}\,\frac{\sigma_{phot,Si}(E)}{\sigma_{tot,Si}(E)}\left(1 - e^{\mu_{Si}(E)\,t_{Si}}\right) \tag{8}$$

where E is the energy of the γ-line, Ω is the solid angle of the detector seen from the source, μ is the linear attenuation coefficient of the material indicated in the subscript, t_{Al} and t_{Si} are, respectively, the thicknesses of the aluminium absorber and of the depleted and intrinsic regions, and, finally, σ_{phot} is the photoelectric and σ_{tot} the total cross section for the interaction of photons, respectively. The values of μ and of the cross sections are taken from NIST Standard Reference Database Number 8 (Berger et al., 2020).

2.4. Choice of a working point

The working point of the BPX 65 is established aiming for the best resolution and efficiency. Concerning the former, two opposite effects are present when the reverse bias is increased in magnitude: the depleted-region capacitance C_T decreases while the reverse current increases. A detailed noise analysis of the detector and the preamplifier has been reported, e.g. by Weinheimer et al. (1992). Looking at their Eq. (3), it is possible to see that decreasing C_T reduces several contributions, while an increase of the reverse current results in a larger associated white noise: therefore two opposite tendencies are present and a minimum of the resolution can appear, as found, e.g. by Bueno et al. (1996, 2004). The electronic contribution to the resolution has been studied, as a function of the reverse bias, employing an Arbitrary

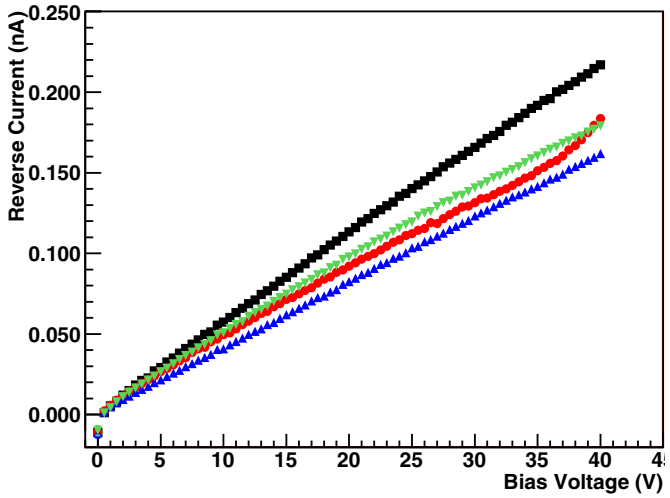

Fig. 1. Reverse current of the four samples of the BPX 65 (sample 1 black (■), sample 2 red (●), sample 3 blue (▲), and sample 4 green (▼)) as a function of the reverse bias. (For interpretation of the references to colour in this figure legend, the reader is referred to the Web version of this article.)

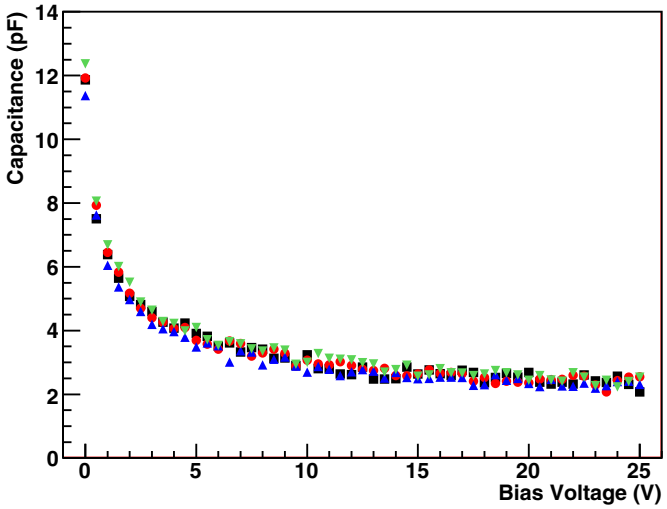

Fig. 2. Depleted-region capacitance C_T of the BPX 65 as a function of the reverse bias. The same four samples used in Fig. 1 have been employed and are reported with the same symbols.

Waveform Generator, simulating a nuclear pulser (see Section 2.3.3). Of course, the detector is kept connected and polarised during these measurements.

Spectra of the ^{241}Am source have also been taken with several bias voltages in the range 0–28 V, and the shape parameters fitted to the observed 26.3 and 59.5 keV γ-ray peaks. Since this device is meant to be used as a particle detector, the resolution and the position of the full-energy peaks are converted from the channel to the energy scale by inverting Eq. (6), which is, strictly, appropriate only for the bias choosen when constructing the calibration. Relative variations are, however, not affected by such a conversion.

3. Results

3.1. Electrical characterisation

The reverse currents of the four samples of BPX 65 have been measured as a function of the applied reverse bias from 0 to 40 V at room temperature. The results are shown in Fig. 1. The standard deviation of the results has been obtained by repeating for one BPX 65 the entire voltage scan five times, and it is ≈ 40% at 0 V, ≈ 5% at 0.5 V, below 4% up to 10 V and below 3% above 10 V. The resulting uncertainty bars are smaller than the size of the symbols and, therefore, are not shown in Fig. 1. The reverse current is approximately linear throughout the voltage range and therefore does not follow the ideal Shockley diode equation (Millman and Halkias, 1972). Its absolute value is well below the typical one declared by the manufacturer (Osram, 2019) (1 nA at 20 V). This is a feature that possibly allowed the samples we tested to perform better than may be possible with other production batches. No signs of pre-breakdown avalanche multiplication are visible in Fig. 1 except maybe for sample 2 above ≈ 35 V. This is in agreement with the datasheet (Osram, 2019) that rates the maximum reverse operating voltage at 20 V for continuous operation and at 50 V for periods of time below 2 min (the entire scan up to 40 V with the B1500A takes few seconds).

The best evaluation of the capacitance of the metallic casing, C_{TO}, measured as described in Section 2.2, is given by the average $C_{TO} = (0.70 \pm 0.07)$ pF of the values measured for the sample with the bond wire removed as a function of reverse bias; the uncertainty is estimated as one standard deviation. This result is compatible with that obtained by Zhao et al. (2016) (0.67 pF and 0.65 pF) and by Zhao et al. (2018) ((0.75 ± 0.01) pF) for the same model of metallic casing. The average C_{TO} mentioned above has been subtracted from the capacitance measured, again at room temperature, for the same four samples of the intact device whose reverse currents are shown in Fig. 1. The final result for C_T, after subtraction of all the parasitic contributions as far as possible, is presented in Fig. 2. The uncertainty on C_T is estimated by propagating the uncertainty on the measurement of the capacitance, evaluated as one standard deviation of the results obtained by repeating five times the entire voltage scan for one particular BPX 65 sample, and the uncertainty on C_{TO} obtained as explained above. It is ≈ 1.3% at 0 V, ≈ 1.8% at 0.5 V, ≈ 6% at 10 V, and up to ≈ 9% at 25 V. The resulting uncertainty bars are smaller than the size of the symbols and, therefore, are again not shown in Fig. 2.

At 0 V, the value of C_T, averaged over all the four samples, is (11.9 ± 0.3) pF (where the uncertainty is estimated as one standard deviation). This is in reasonable agreement with the typical value (11 pF) declared in the datasheet by the manufacturer (Osram, 2019).

Using the results presented in Fig. 2 and $A = 1$ mm^2, W can be calculated from Eq. (1) and is shown in Fig. 3, again as a function of the reverse bias from 0 to 25 V.

The parameters W_0 and V' in Eq. (3) have been fitted to the

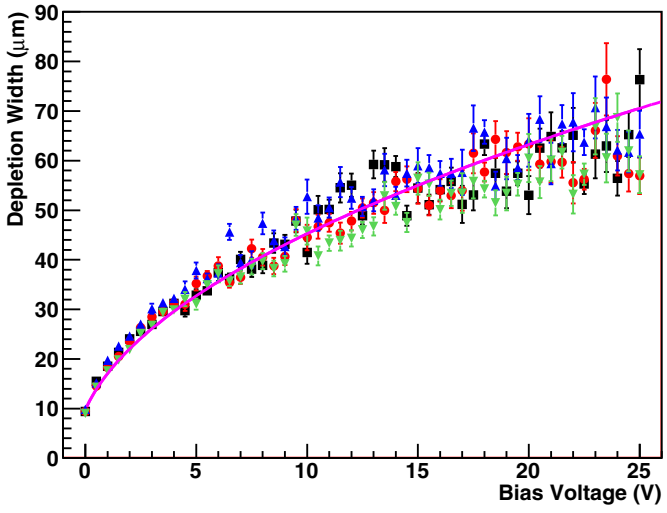

Fig. 3. Total width of the depleted and intrinsic regions, calculated according to Eq. (1), as a function of the reverse bias. The values employed for the depleted-region capacitance C_T are those from Fig. 2. The curve is a plot of Eq. (3) with W_0 and V' fitted to all the data from the four samples.

calculated values of W as a function of V_d, the result being also presented in Fig. 3. The experimental data follow rather well the expected behaviour within the uncertainty bars up to 15–18 V, depending on the sample. Above these voltages, the slope begins to level off. As a matter of fact, Eq. (3) represents the expected behaviour for a PIN junction with infinite p- and n-type regions. The real device stops to follow such a description when getting close to full depletion and deeper layers with different doping concentrations are reached. The values of the parameters estimated from the fit are $V' = (0.487 \pm 0.008)$ V and $W_0 = (9.76 \pm 0.06)$ μm (where the uncertainties are the estimates given by the fit and correspond to one standard deviation). Without knowing the acceptor and donor densities and the thickness of the intrinsic region from the manufacturer, it is not possible to cross check the value of V'. To the best of our knowledge, only one other determination of W_0 for the BPX 65 has been published by Jakšić et al. (2005). Their result is 7.5 μm. Unfortunately, they do not give an uncertainty or describe the method employed: they only mention ion implantation. However, because the manufacturer does not give any detail on the internal structure of the device, it is also possible that the model of the PIN diode with a planar step graded junction may not be totally accurate.

3.2. Working point

The resolution (FWHM), obtained with the pulser, is displayed in Fig. 4 as a function of the reverse bias. The uncertainty bars estimated by the fit are of the order of the size of the symbols and are, therefore, not visible. The selected amplitude of the pulser, when converted to energy by inverting Eq. (6), corresponds to (367.7 ± 0.6) keV. While, initially, increasing the voltage leads to a clear improvement, this effect saturates above ≈ 6 V and no further change is seen afterwards with no sign of a minimum. The dashed horizontal line indicates the value given in Section 3.5 using higher statistics runs at the working point. The white noise produced by the small reverse current of ≈ 0.1 nA at 20 V, found in Section 3.1, has an rms fluctuation of 410 eV FWHM, as it can be calculated employing e.g. Eq. (3) by Weinheimer et al. (1992) and the formation time given in Section 2.3.1. Such a contribution, to be added quadratically to the others to reach the total value shown in Fig. 4, is negligible explaining why there is no minimum. Thus, within the conditions of the present setup, selecting a small size detector with a reduced capacitance is an advantage since it diminishes the impact of other more important terms.

The evolution of the resolution with bias has also been studied with the ^{241}Am source, see Fig. 4. A detailed analysis of the spectra has revealed the clear presence of a spurious peak, corresponding to the well isolated line at 59.5 keV, at energies below the main one (see also item *ii* in Section 2.1). The position of such a structure changes with bias: it finally merges with the main one for 8 V and above. The shape of the spectrum then remains stable for higher voltages over the entire energy range, including the lower part, where well defined peaks are harder to separate. Although it is possible to consider only the main peak produced by 59.5 keV γ-rays, we prefer to restrict the analysis above 8 V. The parameters of the shape model (see Section 2.3.4) have been fitted to regions of the spectra around the full energy peaks corresponding to the 26.3 and the 59.5 keV lines and the FWHM of the Gaussian component is shown in Fig. 4. Again a strong initial reduction is followed by a saturation above 12–14 V with no sign of a minimum, reaching the same value found with the pulser. The 59.5 keV peak is well isolated from all the others with only a small continuum component and the corresponding fit is more stable, as it can be appreciated by both the spread of the points and the size of the uncertainty bars, estimated by the fit and corresponding to one standard deviation, shown in Fig. 4. The situation of the 26.3 keV peak is more complex, as mentioned, since it is located on the shoulder of the structures produced by several lower energy x-rays, see also Section 3.3. It is important to stress that the statistics collected at each voltage to produce Fig. 4 is lower than that collected at the working point for Fig. 7, corresponding to few hours instead of about one day.

Besides the electronic noise, the efficiency also depends on the working point, since, as discussed in Section 3.1, increasing the reverse bias results in larger thicknesses of the depleted and intrinsic regions. In a simple model, where only the charge generated in these parts of the photodiode contributes to the signal, see Eq. (8), a direct influence can be expected, as found, e.g. by Bueno et al. (1996, 2004). This has been tested using again the 26.3 and 59.5 keV peaks from ^{241}Am. The relative efficiency is extracted from the area of the Gaussian component of the shape model, corrected for the live time of the measurement, and is reported, as a function of the reverse bias, in Fig. 5. The values are normalised to 1 at the last point corresponding to 26 V. The uncertainty bars represent the estimates from the fit and correspond to one standard deviation. A strong dependence is observed for 59.5 keV γ-rays at low biases, followed by a slow tendency towards saturation above ≈ 22 V. The situation is very different for 26.3 keV γ-rays, which suffer a much stronger absorption in silicon (i.e. μ_{Si} is larger in Eq. (8)), and reach the saturation efficiency already at ≈ 12 V and above. Note that Fig. 5 reports a relative efficiency, so the absolute efficiency corresponding to 26 V is not necessarily 100%. This is the variable most sensitive to the

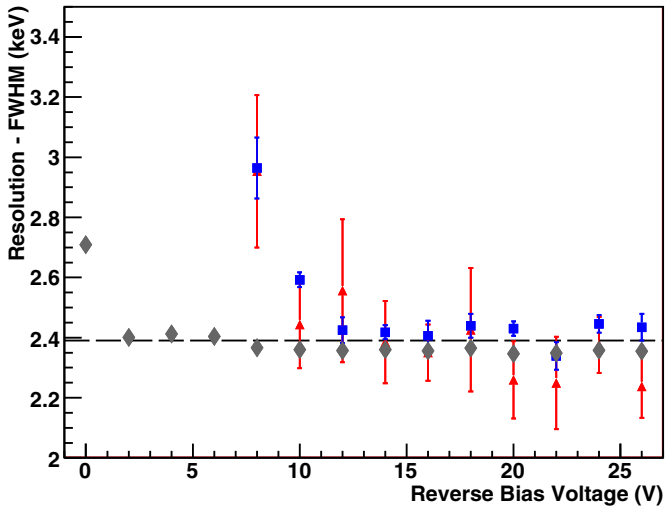

Fig. 4. Resolution (FWHM) as a function of the reverse bias evaluated with the energy calibration from Section 3.4: pulser (◆) and full energy peak corresponding to the 26.3 and 59.5 keV lines from ^{241}Am (▲ and ■, respectively).

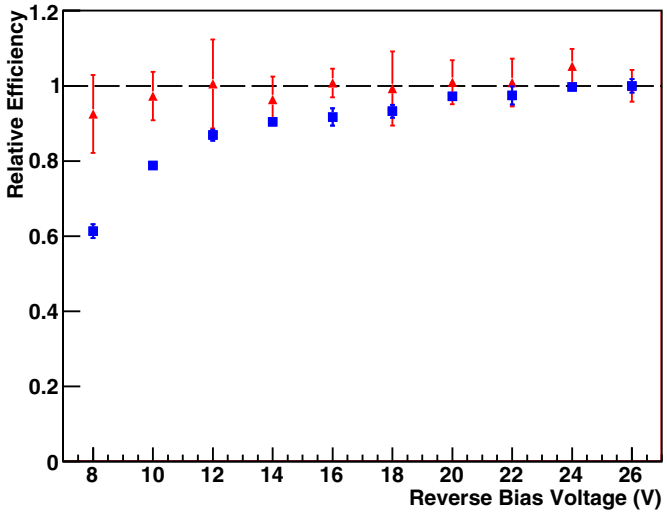

Fig. 5. Relative efficiency of the full energy peak corresponding to the 26.3 and 59.5 keV lines from ^{241}Am (▲ and ■, respectively) as a function of the reverse bias. The values are normalised to one at the highest voltage.

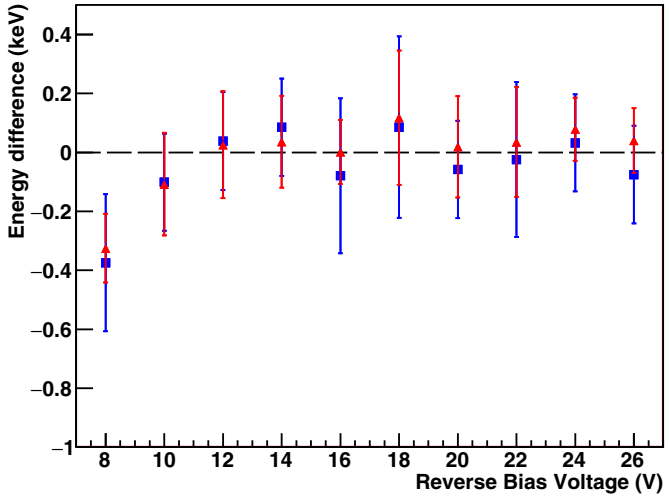

Fig. 6. Position of the full energy peak corresponding to the 26.3 and 59.5 keV lines from ^{241}Am (▲ and ■, respectively), evaluated with the energy calibration from Section 3.4, as a function of the reverse bias.

working point among the three probed here.

A somewhat different, but closely related aspect, is that of the charge-collection efficiency, that is also expected to improve when the reverse bias voltage is increased. This is studied in Fig. 6, where the position of the Gaussian component of the shape model is studied as a function of the reverse bias, again employing the 26.3 and 59.5 keV γ-rays from ^{241}Am. To compare the two different energies, the difference in position with respect to the average between 12 and 26 V is actually reported after conversion to energy by inverting Eq. (6). The uncertainty bars represent the estimates from the fit and correspond to one standard deviation. The behaviour is similar to that shown in Fig. 4 with a clear variation at the beginning and a saturation: above ≈ 12 V there is no dependence visible within the uncertainties of the data.

The operational voltage chosen for all the investigations of the present paper I and of the companion paper II is 18 V, where the shape of the spectrum is well stabilised (no spurious peaks have been found) and the photodiode has already reached its saturation values of the resolution and charge-collection efficiency, but is still comfortably below the maximum rating of 20 V recommended by the manufacturer for steady operation (Osram, 2019). It should be noted that the latter margin refers to a device unaffected by ionising radiation, therefore we preferred a conservative choice remaining 2 V below, even if the photodiode is not fully depleted, on the contrary of commercial devices fabricated to be used as particle detectors. This has the consequence that the efficiency may not have reached its saturation value depending on the energy of the considered photons. The situation for electrons is different, since in that case the issue is not the efficiency but rather the collection of all the deposited energy and is discussed in paper II. No instabilities due to runaway avalanche multiplication have been observed with the choice of a reverse bias of 18 V during all the tests described in the present paper I and in the companion paper II. At the selected working point, according to Eq. (1), the width of the depleted and intrinsic layers is (60 ± 3) μm (which are the average and one standard deviation of the results for the four BPX 65 samples).

To give an idea of the variation between the four samples of BPX 65 examined, it can be said that the capacitance and reverse currents at 18 V vary between 2.30 and 2.64 pF (corresponding with Eq. (1) to $W = 66$ and $W = 54$ μm, respectively) and between 0.08 and 0.11 nA, respectively.

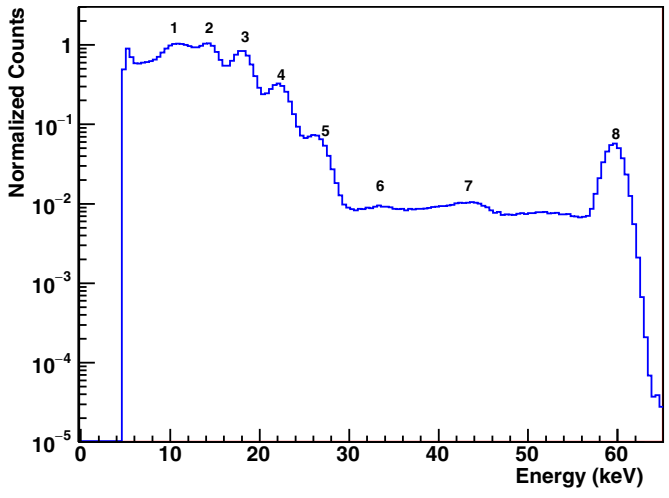

Fig. 7. Spectrum from the ^{241}Am source.

Legend: 1) 11.9 keV x-rays + Compton edge of the 59.9 keV γ-rays, 2) 13.9 keV x-rays, 3) 17.7 keV x-rays, 4) 20.9 keV x-rays, 5) 26.3 keV γ-rays, 6) 33.2 keV γ-rays, 7) edge of x-rays pile-up, 8) 59.5 keV γ-rays. The energy dispersion is 0.33 keV/channel and the vertical scale has been normalised so that the maximum of peak 1 is 1.

3.3. Photon spectra

The spectra obtained with the ^{241}Am, ^{133}Ba, and ^{57}Co sources are shown in Figs. 7–9, respectively. The vertical scales have been normalised so that the maximum of the most intense γ- or x-ray peak, among those identified, which is indicated with the number 1 in Figs. 7–9, is 1.

The ^{241}Am source, described in Section 2.3.2, has been placed in the arrangement with the thick support between the radioactive nuclides and the detector to stop the charged particles, therefore all the peaks visible in Fig. 7 can be associated to photon emission lines. To ease the procedure, the chamber has been kept in air at ambient pressure and temperature because a small reduction of the photon intensity is

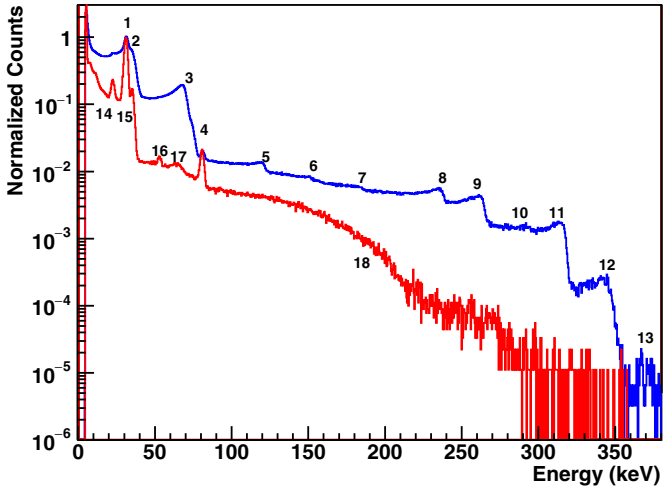

Fig. 8. Spectra from the ^{133}Ba source: less intense (red line) with the Al absorber, and more intense (blue line) without, therefore only the Kapton-foil cover of the source absorbed the photons and displaced the peaks corresponding to electron conversion lines from their emission energies.

Legend: 1) 30.9 keV x-rays, 2) 45.0 keV electrons +35.1 keV x-rays, 3) 74–81 keV electrons +53.2 keV γ-rays, 4) 81.0 keV γ-rays, 5) 125 keV electrons, 6) 155 keV electrons 7) 187 keV electrons, 8) 240 keV electrons, 9) 267 keV electrons, 10) 298 keV electrons, 11) 320 keV electrons, 12) 350 keV electrons, 13) 378 keV electrons, 14) 22.0 keV Ag x-rays, 15) 35.1 keV x-rays, 16) 53.2 keV γ-rays, 17) Backscattering of 81.0 keV γ-rays, 18) Compton edge of the 356 keV γ-rays. The energy dispersion is 0.33 keV/channel and the vertical scale has been normalised so that the maximum of peak 1 is 1. (For interpretation of the references to colour in this figure legend, the reader is referred to the Web version of this article.)

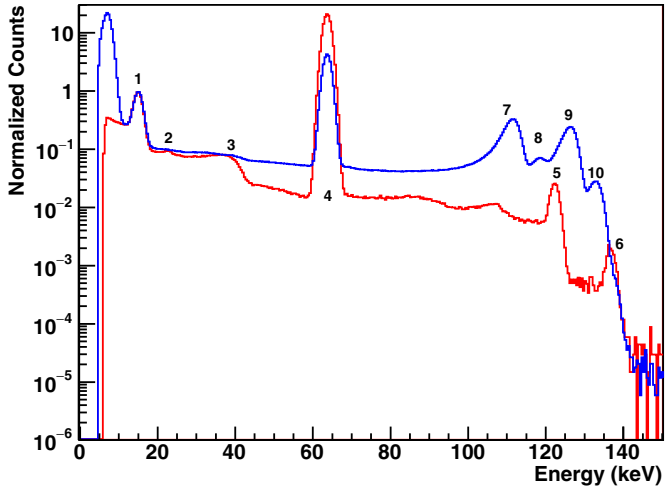

Fig. 9. Same as Fig. 8, but for the ^{57}Co source.

Legend: 1) 14.4 keV γ-rays, 2) 22.0 keV Ag x-rays, 3) Compton edge of 122 keV, 4) pulser, 5) 122 keV γ-rays, 6) 136 keV γ-rays, 7) 115 keV electrons, 8) 121 keV electrons, 9) 129 keV electrons, 10) 136 keV electrons.

irrelevant for the present purpose. Since the enclosing of the ^{133}Ba and ^{57}Co sources are thin, see Section 2.3.2, the peaks visible in Figs. 8 and 9 can correspond to both photon or electron emission lines (the chamber has been maintained under vacuum at a pressure of 7 mPa for these two measurements). Initially, it has been hoped that the response of the BPX 65 to electrons could be investigated in such a way. Unfortunately, the electrons from internal conversion loose some energy in the Kapton-foil cover of the source and therefore appear displaced with respect to the corresponding photons. This complexity makes it difficult to interpret the data. Therefore, other spectra have been acquired interposing a 0.5 mm-thick Al foil between the detector and the ^{133}Ba and ^{57}Co sources to fully stop all the electrons with the energies expected from their decays (again, to ease the procedure, the chamber has been left in air at atmospheric pressure). These new spectra are also shown in Figs. 8 and 9: now the peaks correspond to photon emission lines only (again the maximum of the most intense identified one has been normalised to 1). The use of the absorber greatly reduces the continuum component as well, indicating that electrons are its main origin. Note that for the ^{57}Co source, the pulser, employed to monitor the stability of the electronic chain, see Section 2.3.3, has been adjusted to produce a peak in the region between 50 and 100 keV, where there are no interesting structures, as can be seen in Fig. 9. In the cases of the ^{241}Am and ^{133}Ba spectra, the peak from the pulser is located outside the range of the figures.

Two typical fits of the parameters of the peak shape model (see Section 2.3.4) to the spectra measured with ^{133}Ba and ^{57}Co sources are shown in Figs. 10 and 11, respectively. The continuous black line is the result of the complete fit including the γ-ray transitions. The dashed line represents the continuum component alone: the effect of the terms corresponding to Eq. (5) is clear in both Figs. 10 and 11. The structure visible in Fig. 10 around 63 keV is not a line but corresponds to the backscattering of γ-rays with an energy of 81.0 (79.6) keV. A Gaussian has been added to model the spectrum over the whole energy range of Fig. 10, but the fitted parameters are not employed in what follows. The case of the peak at 81.0 keV requires special attention because it is actually the result of two transitions, one at 81.0 keV and another at 79.6 keV, that are closer than the detector resolution and, therefore, do not appear as separated. Two Gaussians have been introduced in the fit. To reduce the number of parameters, the following three constraints are imposed (only for this particular case). 1) The ratio of the intensities $A_{G\,1}/A_{G\,2}$, see Eq. (4), is fixed to the value given by Bé et al. (2016), so that only one overall normalisation remains variable. The standard deviations of the two Gaussians are the same, i.e. $\sigma_{G\,1} = \sigma_{G\,2}$. The

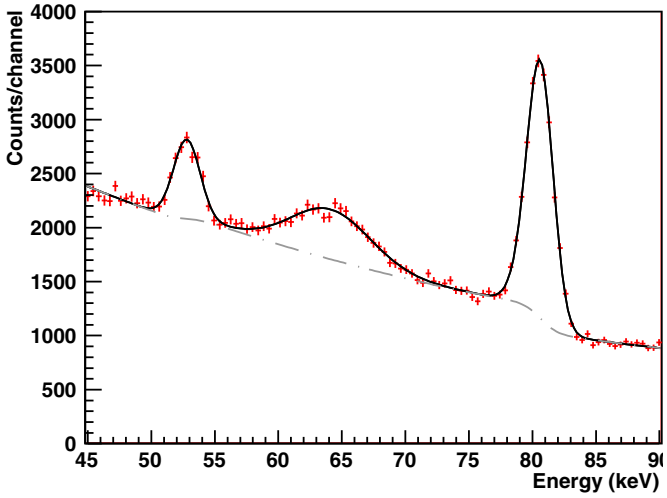

Fig. 10. The points with the uncertainty bars represent the selected region of the photon emission spectrum from the ^{133}Ba source encompassing the lines at 53.2, 79.6, and 81.0 keV. The continuous (black) line shows the model described in Section 2.3.4 with the fitted parameters, while the dashed (grey) line displays the continuum component alone of this model. The energy dispersion is 0.33 keV/channel.

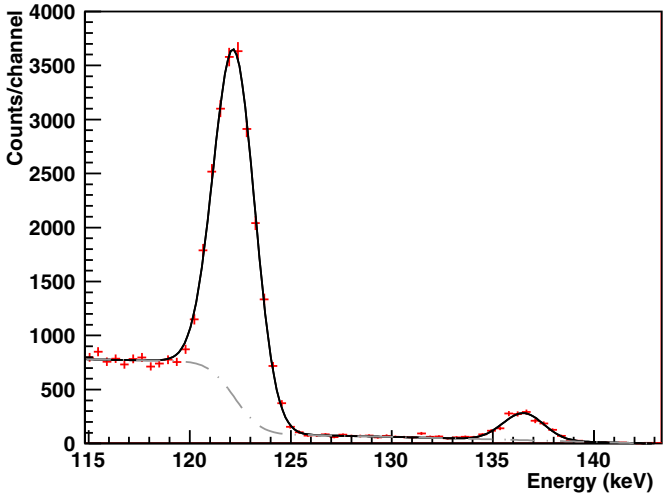

Fig. 11. Same as Fig. 10, but for the ^{57}Co source, showing the photon emission lines at 122 and 136 keV.

difference in the position of the two peaks, $x_{G\,2} - x_{G\,1}$, is fixed according to the tabulated (Bé et al., 2016) energy difference of the two lines. Note that this requires an iterative procedure because knowledge of the energy to channel conversion factor is needed. Due to the large difference in intensity, the convergence is very fast and only two repetitions are needed. Finally, one more simplification is introduced in the description of the continuum component: only one term like Eq. (5), corresponding to the energy of the most intense line, is added. Even accounting for these assumptions, the fit shown in Fig. 10 has 14 free parameters.

3.4. Energy calibration

A linear calibration has been performed according to Eq. (6). The peak positions of the selected γ-lines have been obtained in Section 3.3 with the fitting procedure described in Section 2.3.4 from the spectra collected with the ^{241}Am, ^{133}Ba, and ^{57}Co sources. They are shown in the upper panel of Fig. 12. The low-energy structures visible in Figs. 8 and 9 have not been included in the LS procedure because they

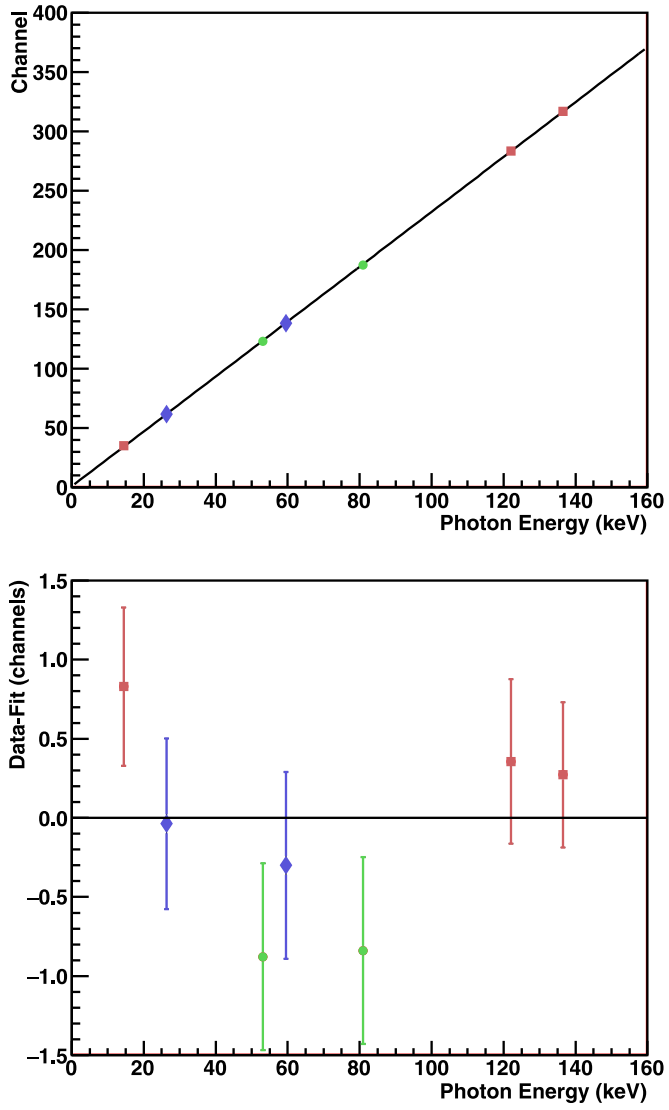

Fig. 12. Upper panel: peak positions versus energy of the γ-transitions selected for the calibration. The black line is the linear relation, Eq. (6), with the parameters from a fit. Lower panel: residuals of the fit. The sources are represented with different symbols (^{241}Am ◆, ^{133}Ba ●, and ^{57}Co ■).

correspond to multiple x-rays transitions that are not well separated and do not help in improving the accuracy of the result. The uncertainties on the positions of the peaks from the fit to the spectra tend to be quite different depending on the intensity of emission and the detector efficiency. Thus, to avoid biasing the calibration towards some particular points, we prefer to use as uncertainty on the positions of the peaks the standard deviation of the residuals of the fit with Eq. (6). We have then been able to clearly uncover a systematic trend (see below). The parameters determined in such a way with their uncertainties are $a = (0.9 \pm 0.4)$ channels and $b = (2.313 \pm 0.005)$ channels/keV. The deviations of the peak positions from the expectations of Eq. (6) with the values of a and b given above, are plotted in the lower panel of Fig. 12. It is clear that the spectroscopy chain has a tendency to drift by ≈ 1 channel in 1024 from ^{133}Ba to ^{241}Am and then of roughly the same amount from ^{241}Am to ^{57}Co, limiting the precision of the present calibration. However, improving the situation would require a better pulser capable of generating a sequence of different amplitudes to correct variations in both gain and offset.

Applying such a calibration curve to all the spectra in Figs. 7–9, the other x-ray, γ-ray, and internal conversion peaks, not used in its construction, can be identified. The results are presented in the captions of Figs. 7–9. In the case of electrons, the energy lost in the Kapton foil covering the sources has been estimated adopting the total stopping power from the ESTAR database (Berger et al., 2017) and added to the energy determined with the calibration curve to identify the peak.

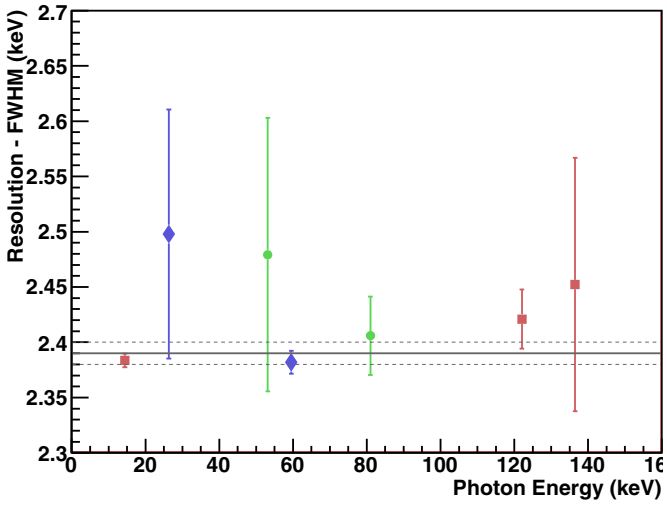

Fig. 13. Resolution (FWHM) as a function of the energy. The points with uncertainty bars are from the peaks observed with the ^{241}Am (◆), ^{133}Ba (●), and ^{57}Co (■) sources. The grey continuous horizontal line represents the value measured with the pulser during the same runs with the corresponding uncertainty bar given by the thin dashed lines.

3.5. Dependence of the resolution on photon energy

The energy resolution (FWHM) of the BPX 65, evaluated from the standard deviation of the Gaussian component fitted to the observed spectra, see Section 2.3.4 and 3.3, is shown in Fig. 13 as a function of the energy, selecting only γ-rays. The uncertainty bars are the estimates from the fit and correspond to one standard deviation. The resolution is practically constant throughout the evaluated energy range (14–136 keV), being rather close, within the uncertainties, to that of (2.39 ± 0.01) keV obtained with the pulser during the same runs (where the value and the uncertainty are the mean and its standard deviation for the ^{241}Am, ^{133}Ba, and ^{57}Co runs). Therefore, it is possible to conclude that, in the setup employed here, the main limiting factor is the noise from the electronic chain. This is fully consistent with the magnitude of the energy dependence given in Section 2.3.6 being negligible. Moreover, no margin is left for a relevant role of fluctuations in the charge collection efficiency. The result shown in Fig. 13 for the BPX 65 using the γ-rays emitted by ^{241}Am at 59.5-keV is (2.38 ± 0.01) keV (where the uncertainty is the estimate given by the fit and correspond to one standard deviation), rather similar to that of other PIN photodiodes available commercially (Ahmad et al., 1990; Bueno et al., 1996, 2004).

3.6. Photon efficiency

The areas of the peaks corresponding to γ-lines in Figs. 8 and 9 have been compared to the expectations from Eq. (8). The calculated and measured values for energies between 14.4 and 136 keV agree within 20%, which is of the order of the uncertainties in the determination of Ω. Moreover, since the source has been placed at about 1 cm from the detector, it can not be considered to be point-like and corrections are necessary in the evaluation of Ω that are difficult to determine. It has also been verified that the more refined model by Seltzer (1981), as implemented by Barros et al. (2017), gives, for the present case where $t_{Si} = 60$ μm, an efficiency indistinguishable from Eq. (8).

Zhao et al. (2018) and Wall et al. (2014) presented experimental evidences that, in PIN diodes, minority charge carriers generated in the entrance dead layer diffuse to the active region and contribute to the signal for impinging photons and electrons, respectively. In particular, Zhao et al. (2016) employed 5.9-keV γ-rays from a calibrated radioactive source and the thickness of the active layer in their devices was of the order of a few microns, about one order of magnitude less than in the present case. Here, the thickness of the dead layer estimated in paper II is of the order of tenths of microns. Thus, the effect of a partially dead layer for photons is much smaller than the accuracy reached by the analysis described above with Eq. (8). The situation is different for electrons because they start to loose energy as soon as they impinge on the front face of the detector, while photon interactions are randomly distributed within it. Similar arguments apply to the case of minority charge carriers produced in the undepleted part of the diode on the back side of the depleted and intrinsic regions: they can also possibly contribute to the signal by diffusion. These issues are treated in more detail in paper II where they can be analysed more directly with electrons.

4. Discussion

The thickness of the depleted and intrinsic layers of (60 ± 3) μm at the selected working point of 18 V matches the range calculated in the continuous slowing down approximation (CSDA) for electrons with a kinetic energy of 85 keV. If electrons with kinetic energies up to this value hit the detector, they are expected to stop inside the depleted and intrinsic regions resulting in a full collection of all the generated charge carriers. In practice, electrons interacting with the detector material do not follow straight trajectories because of multiple scattering and therefore the process of energy deposition is much more complex than it is described by the CSDA. The response function to monoenergetic electrons is analysed in detail in paper II (Mangiarotti et al., 2020). Here it is worth noting that, when the primary particle is a photon, to produce an electric signal, it is first necessary that a fraction or all of its energy is transferred to electrons of an atom of the detector material by photoelectric effect or Compton scattering. Because the impinging photon can undergo the first interaction at any point in the detector material, the issue of fully containing all the secondary electrons in the depleted and intrinsic regions becomes even more complex. A constant efficiency is reached below the selected working point when employing 26.3 keV γ-rays, see Fig. 5, which is consistent with an inverse linear attenuation coefficient of $1/\mu_{Si} = 4.5$ μm (Berger et al., 2020). The situation is already different for 59.5 keV γ-rays where $1/\mu_{Si} = 37$ μm and the saturation is not encountered at 18 V. Both the electronic noise and the charge collection efficiency are not affected by the number of generated charge carriers. Thus, the behaviours shown in Figs. 4 and 6 do not change significantly for photons of different energies. As a matter of fact, the signals from the pulser visible in Fig. 4 have an amplitude ≈ 6 times larger than that produced by 59.5 keV γ-rays, see Section 3.2, but again show saturation at the selected working point. Since the BPX 65 is not intended for particle detection, it can not be operated in an overdepleted condition and the efficiency for photons with energies above 30–40 keV remains sensitive to the thickness of the active volume and, therefore, to the selected working point (e.g. for 100 keV γ-rays, $1/\mu_{Si} = 64$ μm (Berger et al., 2020), which is comparable to the thickness of the depleted and intrinsic regions). However, the criterion of remaining below the maximum rating of 20 V, mentioned in Section 3.2, should not be violated leaving a small margin available for improvement.

No spurious peaks have been identified in all the spectra shown in Figs. 7–9, therefore excluding important effects of incomplete charge collection at the selected working point. Moreover, well defined peaks are clearly visible in Fig. 9 for γ-rays with energies of 122 and 136 keV, although with a low efficiency (the former is the most intense emission accounting for, on average, 85.5 photons per hundred decays (Bé et al., 2004)). Nevertheless, there is no evidence of a worse resolution for 122 and 136 keV in Fig. 13. Thus, the detector can eventually be used for photons with energies up to ≈ 140 keV, although with a small efficiency.

5. Conclusion

A commercial PIN photodiode has been identified and characterised to measure the energy spectra of electrons scattered by thin metallic foils close to the beam of an accelerator. Its main features are: 1) a low-cost solution to allow frequent replacements; 2) a small size to avoid as much as possible an unused area that contributes with unnecessary capacitance; 3) a good energy resolution; and 4) an easy repurposing as a charged-particle detector. The BPX 65 satisfies all these requirements. Its TO-18 metallic casing allows for a simple preparation, its active area is 1 mm^2 (well matched to the anticipated size of the collimator hole with a diameter of 0.5 mm) and its cost is about two orders of magnitude lower then that of a commercial surface barrier or passivated implanted planar silicon (PIPS) detector. The working point has been chosen at 18 V, comfortably below the maximum rating of 20 V recommended by the manufacturer (Osram®) for steady operation. The reverse currents, measured at a reverse bias of 18 V for the four samples tested, are around 0.1 nA, well below the typical value specified by the manufacturer (1 nA). The total thickness of the depleted and intrinsic regions, obtained from measurements of the depleted-region capacitance, again at a reverse bias of 18 V, is (60 ± 3) μm. The performance of the device as a photon detector for energies between 10 and 140 keV has been investigated. Despite the low efficiency, the energy resolution, obtained with the γ-rays emitted by ^{241}Am at 59.5-keV, is (2.38 ± 0.01) keV, quite comparable to that of other commercial PIN photodiodes operated at room temperature and slightly better than that obtained in our tests with a PIPS detector. The main limitation for its resolution is the noise from the electronic chain, which could in principle be improved by a better preamplifier and coupling or by cooling the BPX 65 and the first stage of the preamplifier. The energy calibration curve, applied to all measured spectra, allowed the correct identification of peaks other than those selected for its construction, including peaks from internal conversion electrons emitted by ^{133}Ba and ^{57}Co. This indicates that the BPX 65 is a good candidate for electron spectrometry. Nevertheless, electrons produced from these sources, even when especially covered with thin Kapton foils, still loose energy and are not well suited to study the response function. This task is undertaken in accompanying paper II (Mangiarotti et al., 2020), where the monoenergetic beam from an electron accelerator is used.

CRediT authorship contribution statement

A.A. Malafronte: Methodology, Resources, Investigation, Data curation, Formal analysis. **A.R. Petri:** Methodology, Investigation, Data curation, Formal analysis, Visualization. **J.A.C. Gonçalves:** Methodology, Resources, Investigation, Formal analysis, Funding acquisition. **S.F. Barros:** Methodology, Formal analysis. **C.C. Bueno:** Methodology, Formal analysis, Funding acquisition. **N.L. Maidana:** Methodology, Formal analysis, Funding acquisition. **A. Mangiarotti:** Conceptualization, Methodology, Formal analysis, Writing - original draft, Writing - review & editing, Project administration, Funding acquisition. **M.N. Martins:** Methodology, Formal analysis, Writing - review & editing, Funding acquisition. **A.A. Quivy:** Methodology, Resources, Investigation, Funding acquisition. **V.R. Vanin:** Methodology, Formal analysis, Writing - review & editing, Funding acquisition.

Declaration of competing interest

The authors declare that they have no known competing financial

interests or personal relationships that could have appeared to influence the work reported in this paper.

Acknowledgements

The authors are grateful to Profa. Dra. Marina Fallone Koskinas from Instituto de Pesquisas Energéticas e Nucleares (IPEN), São Paulo, for manufacturing of the ^{133}Ba and ^{57}Co sources. This work has been funded by Fundação de Amparo à Pesquisa do Estado de São Paulo (FAPESP) under Contract No. 2016/13116–5 and by Instituto de Pesquisas Energéticas e Nucleares, Comissão Nacional de Energia Nuclear (IPEN-CNEN) under contract DPDE Edital April 2017. ARP acknowledges a fellowship by FAPESP, under Contract No. 2017/12661–2. AM and AAQ acknowledge support by Conselho Nacional de Desenvolvimento Científico e Tecnológico (CNPq) under Contracts No. 306331/2016–0 and 311687/2017–2, respectively.

Appendix A. Supplementary data

Supplementary data to this article can be found online at https://doi.org/10.1016/j.radphyschem.2020.109103.

References

Abramowitz, M., Stegun, I.A., 1972. Handbook of Mathematical Functions with Formulas, Graphs and Mathematical Tables, ninth ed. Dover, New York, USA.

Ahmad, I., Betts, R.R., Happ, T., Henderson, D.J., Wolfs, F.L.H., Wuosmaa, A.H., 1990. Nuclear spectroscopy with Si PIN diode detectors at room temperature. Nucl. Instrum. Methods Phys. Res. 299, 201–204.

Barros, S.F., Maidana, N.L., Fernández-Varea, J.M., Vanin, V.R., 2017. Full-energy peak efficiency of Si drift and Si(Li) detectors for photons with energies above the Si K binding energy. X Ray Spectrom. 46, 34–43.

Bé, M.-M., Chisté, V., Dulieu, C., Browne, E., Chechev, V., Kuzmenko, N., Helmer, R., Nichols, A., Schönfeld, E., Dersch, R., 2004. of Monographie BIPM-5. Table of Radionuclides, vol. 1 Bureau International des Poids et Mesures, Pavillon de Breteuil, F-92310 Sèvres, France. http://www.bipm.org/utils/common/pdf/monographieRI/Monographie_BIPM-5_Tables_Vol1.pdf.

Bé, M.-M., Chisté, V., Dulieu, C., Kellett, M.A., Mougeot, X., Arinc, A., Chechev, V.P., Kuzmenko, N.K., Kibédi, T., Luca, A., Nichols, A.L., 2016. of Monographie BIPM-5. Table of Radionuclides, vol. 8 Bureau International des Poids et Mesures, Pavillon de Breteuil, F-92310 Sèvres, France. http://www.bipm.org/utils/common/pdf/monographieRI/Monographie_BIPM-5_Tables_Vol8.pdf.

Bé, M.-M., Chisté, V., Dulieu, C., Mougeot, X., Browne, E., Chechev, V., Kuzmenko, N., Kondev, F., Luca, A., Galán, M., Nichols, A.L., Arinc, A., Huang, X., 2010. of Monographie BIPM-5. Table of Radionuclides, vol. 5 Bureau International des Poids et Mesures, Pavillon de Breteuil, F-92310 Sèvres, France. http://www.bipm.org/utils/common/pdf/monographieRI/Monographie_BIPM-5_Tables_Vol5.pdf.

Berger, M.J., Coursey, J.S., Zucker, M.A., Chang, J., 2017. Stopping-Power & Range Tables for Electrons, Protons, and Helium Ions, NIST Standard Reference Database Number 124. National Institute of Standards and Technology, Gaithersburg MD. https://doi.org/10.18434/T4NC7P. 20899.

Berger, M.J., Hubbell, J.H., Seltzer, S.M., Chang, J., Coursey, J.S., Sukumar, R., Zucker, D.S., Olsen, K., 2020. XCOM: Photon Cross Section Database Version 1.5, NIST Standard Reference Database Number 8. National Institute of Standards and Technology, Gaithersburg MD. https://doi.org/10.18434/T48G6X. 20899.

Brun, R., Rademakers, F., 1997. Root – An object oriented data analysis framework. Nucl. Instrum. Methods Phys. Res. 389, 81–86.

Bueno, C.C., Gonçalves, J.A.C., de S Santos, M.D., 1996. The performance of low-cost commercial photodiodes for charged particle and X-ray spectrometry. Nucl. Instrum. Methods Phys. Res. 371, 460–464.

Bueno, C.C., Gonçalves, J.A.C., Magalhães, R.R., Santos, M.D.S., 2004. Response of PIN diodes as room temperature photon detectors. Appl. Radiat. Isot. 61, 1343–1347.

Gao, F., Campbell, L.W., Devanathan, R., Xie, Y., Corrales, L.R., Peurrung, A.J., Weber, W.J., 2007. Monte Carlo method for simulating γ-ray interaction with materials: A case study on Si. Nucl. Instrum. Methods Phys. Res. 579, 292–296.

Gonçalves, J.A.C., Mangiarotti, A., Bueno, C.C., 2020. Current response stability of a commercial PIN photodiode for low dose radiation processing applications. Radiat. Phys. Chem. 167, 108276.

Gooda, P.H., Gilboy, W.B., 1987. High resolution alpha spectroscopy with low cost photodiodes. Nucl. Instrum. Methods Phys. Res. 255, 222–224.

Hollstein, M., 1970. Response characteristics of a high-resolution Si(Li) photon spectrometer. Nucl. Instrum. Methods 82, 249–252.

Jafari, H., Feghhi, S.A.H., Boorboor, S., 2018. Evaluation of gamma dose effect on PIN photodiode using analytical model. Radiat. Phys. Chem. 144, 379–385.

Jakšić, M., Medunić, Z., Bogovac, M., Skukan, N., 2005. Radiation damage microstructures in silicon and application in position sensitive charged particle detection. Nucl. Instrum. Methods Phys. Res. B 231, 502–506.

James, F., Roos, M., 1975. Minuit - a system for function minimization and analysis of the parameter errors and correlations. Comput. Phys. Commun. 10, 343–367.

Khoury, H.J., Hazin, C.A., Mascarenhas, A.P., da Silva Jr., E.F., 1999. Low cost silicon photodiode for electron dosimetry. Radiat. Protect. Dosim. 84, 341–343.

Khoury, H.J., Schelin, H., Soboll, D., Lunelli, N., Baptista, C., 2007. Evaluation of commercial silicon diode for electron dosimetry. Nucl. Instrum. Methods Phys. Res. 580, 537–539.

Knoll, G.F., 2010. Radiation Detection and Measurement, fourth ed. Wiley, New York, USA.

Kollewe, D., 1987. Performance of 10×10 mm^2 PIN silicon photocells used as high resolution charged particle detectors. Nucl. Instrum. Methods Phys. Res. 254, 637–638.

Lee, S.C., Jeon, H.B., Kang, K.H., Park, H., 2016. Study of silicon PIN diode responses to low energy gamma-ray. J. Kor. Phys. Soc. 69, 1587–1590.

Mangiarotti, A., Petri, A.R., Malafronte, A.A., Gonçalves, J.A.C., Barros, S.F., Bueno, C.C., Fernández-Varea, J.M., Maidana, N.L., Martins, M.N., Vanin, V.R., 2020. A low-cost small-size commercial PIN photodiode: II. comparison of measurements with monoenergetic electrons to analytical expressions and Monte Carlo simulations. Radiat. Phys. Chem. Vol.

Markevich, I., Gertner, I., Felsteiner, J., 1988. H^+ and He^+ spetroscopy using PIN photodiodes. Nucl. Instrum. Methods Phys. Res. 269, 599–602.

Millman, J., Halkias, C.H., 1972. Integrated Electronics: Analog and Digital Circuits and Systems, first ed. McGraw-Hill, Inc., USA.

Oliveira, C.N.P., Khoury, H.J., Santos, E.J.P., 2016. Pin photodiode performance comparison for dosimetry in radiology applications. Phys. Med. 32, 1495–1501.

Osram, 2019. Metal Can® TO18 BPX65. https://www.osram.com/ecat/Metal%20Can%c2%ae%20TO18%20BPX%2065/com/en/class_pim_web_catalog_103489/global/prd_pim_device_2219550/.

Owens, A., 1985. Spectral degradation effects in an 86 cm$_3$ Ge(HP) detector. Nucl. Instrum. Methods Phys. Res. 238, 473–478.

Palni, P., Hoeferkamp, M., Taylor, A., Vora, S., McDuff, H., Gu, Q., Seidel, S., 2014. A method for real time monitoring of charged particle beam profile and fluence. Nucl. Instrum. Methods Phys. Res. 735, 213–217.

Romei, C., Di Fulvio, A., Traino, C.A., Ciolini, R., d'Errico, F., 2015. Characterization of a low-cost pin photodiode for dosimetry in diagnostic radiology. Phys. Med. 31, 112–116.

Scholze, F., Procop, M., 2001. Measurement of detection efficiency and response functions for an Si(Li) x-ray spectrometer in the range 0.1–5 keV. X Ray Spectrom. 30, 69–76.

Seltzer, S.M., 1981. Calculated response of intrinsic germanium detectors to narrow beams of photons with energies up to ≈ 300 kev. Nucl. Instrum. Methods 188, 133–151.

Wall, B.L., Amsbaugh, J.F., Beglarian, A., Bergmann, T., Bichsel, H.C., Bodine, L.I., Boyd, N.M., Burritt, T.H., Chaoui, Z., Corona, T.J., Doe, P.J., Enomoto, S., Harms, F., Harper, G.C., Howe, M., Martin, E.L., Parno, D.S., Peterson, D., Petzold, L., Renschler, P., Robertson, R.G.H., Schwarz, J., Steidl, M., Van Wechel, T.D., Devender, B.A.V., Wüstling, S., Wierman, K.J., Wilkerson, J., 2014. Dead layer on silicon p–i–n diode charged-particle detectors. Nucl. Instrum. Methods Phys. Res. 744, 73–79.

Weinheimer, C., Schrader, M., Bonn, J., Loeken, T., Backe, H., 1992. Measurement of energy resolution and dead layer thickness of LN_2-cooled PIN photodiodes. Nucl. Instrum. Methods Phys. Res. 311, 273–279.

Yamamoto, H., Hatakeyama, S., Norimura, T., Tsuchiya, T., 1988. Low energy nuclear radiation detection with a silicon photodiode. Nucl. Instrum. Methods Phys. Res. 281, 128–132.

Zhao, S., Gohil, T., Lioliou, G., Barnett, A.M., 2016. Soft X-ray detection and photon counting spectroscopy with commercial 4H-SiC Schottky photodiodes. Nucl. Instrum. Methods Phys. Res. 830, 1–5.

Zhao, S., Lioliou, G., Barnett, A.M., 2018. X-ray spectrometer with a low-cost SiC photodiode. Nucl. Instrum. Methods Phys. Res. 887, 138–143.